The MAGPI Survey: Massive slow rotator population in place by $z \sim 0.3$

Caro Derkenne, ^{1,2} Richard M. McDermid, ^{1,2} Francesco D'Eugenio, ^{3,4} Caroline Foster, ^{2,5} Aman Khalid, ^{2,5} Katherine E. Harborne, ^{2,6} Jesse van de Sande^{2,7}, Scott M. Croom, ^{2,7}, Claudia D.P. Lagos, ^{2,6} Sabine Bellstedt, ⁶ J. Trevor Mendel, ^{2,8} Marcie Mun^{2,8} Emily Wisnioski, ^{2,8} Ryan S. Bagge^{2,5} Andrew J. Battisti, ^{2,8} Joss Bland-Hawthorn, ⁷ Anna Ferré-Mateu, ^{9,10,11} Yingjie Peng^{12,13} Giulia Santucci, ^{2,6} Sarah M. Sweet^{2,14}, Sabine Thater¹⁵, Lucas M. Valenzuela¹⁶, and Bodo Ziegler¹⁵

¹Astrophysics and Space Technologies Research Centre, School of Mathematical and Physical Sciences, Macquarie University, NSW 2109, Australia

²ARC Centre of Excellence for All Sky Astrophysics in 3 Dimensions (ASTRO 3D), Australia

³ Kavli Institute for Cosmology, University of Cambridge, Madingley Road, Cambridge, CB3 0HA, United Kingdom

 4 Cavendish Laboratory - Astrophysics Group, University of Cambridge, 19 JJ Thomson Avenue, Cambridge, CB3 0HE, United Kingdom

⁵School of Physics, University of New South Wales, Sydney, NSW 2052, Australia

⁶International Centre for Radio Astronomy Research, The University of Western Australia, 35 Stirling Highway, Crawley, WA 6009, Australia

⁷Sydney Institute for Astronomy, School of Physics, University of Sydney, NSW 2006, Australia

Research School of Astronomy and Astrophysics, Australian National University, Canberra, ACT 2611, Australia

⁹Instituto de Astrofísica de Canarias, Vía Láctea s/n, E-38205 La Laguna, Tenerife, Spain

¹⁰Departamento de Astrofisica, Universidad de La Laguna, E-38200, La Laguna, Tenerife, Spain

¹¹Center for Astrophysics and Supercomputing, Swinburne University, John Street, Hawthorn, VIC 3122, Australia

¹²Department of Astronomy, School of Physics, Peking University, 5 Yiheyuan Road, Beijing 100871, People's Republic of China

¹³Kavli Institute for Astronomy and Astrophysics, Peking University, 5 Yiheyuan Road, Beijing 100871, People's Republic of China

¹⁴School of Mathematics and Physics, University of Queensland, Brisbane, QLD 4072, Australia

¹⁵Department of Astrophysics, University of Vienna, Türkenschanzstrasse 17, 1180 Wien, Austria

Accepted XXX. Received YYY; in original form ZZZ

ABSTRACT

We use the 'Middle Ages Galaxy Properties with Integral field spectroscopy' (MAGPI) survey to investigate whether galaxies have evolved in the distribution of their stellar angular momentum in the past 3-4 Gyr, as probed by the observational proxy for spin, λ_R . We use 2D stellar kinematics to measure λ_R along with detailed photometric models to estimate galaxy ellipticity. The combination of these measurements quantifies the kinematic classes of 'fast rotators' and the rarer 'slow rotators', which show no regular rotation in their line-of-sight velocity fields. We compare 51 MAGPI galaxies with $\log_{10}(M_{\star}/M_{\odot}) > 10$ to carefully drawn samples of MaNGA galaxies in the local Universe, selected to represent possible descendants of the MAGPI progenitors. The EAGLE simulations are used to identify possible evolutionary pathways between the two samples, explicitly accounting for progenitor bias in our results and the varied evolutionary pathways a galaxy might take between the two epochs. We find that the occurrence of slow rotating galaxies is unchanged between the MAGPI ($z \sim 0.3$) and MaNGA ($z \sim 0$) samples, suggesting the massive slow rotator population was already in place ~ 4 Gyr ago and has not accumulated since. There is a hint of the MAGPI sample having an excess of high λ_R galaxies compared to the MaNGA sample, corresponding to more ordered rotation, but statistically the samples are not significantly different. The large-scale stellar kinematics, as quantified through the λ_R parameter, of galaxies at $z \sim 0.3$ have already evolved into the diversity of structures seen today in the local Universe.

Key words: galaxies: evolution – galaxies: kinematics and dynamics

1 INTRODUCTION

Integral field spectroscopy (IFS) allows us to observe a wealth of detail in the kinematic structure of galaxies, unlocking their histories

through their stellar motions (Cappellari 2016). Of particular interest is assessing the relative amounts of ordered and random motions within a galaxy, as this kinematic signature can encode the various accretion and merger events a galaxy has experienced (Naab et al. 2014; Lagos et al. 2018b). One method of quantifying the relative amount of pressure and rotation support in a galaxy is to measure

¹⁶Universitäts-Sternwarte, Fakultät für Physik, Ludwig-Maximilians-Universität München, Scheinerstr. 1, 81679 München, Germany

^{*} E-mail:richard.mcdermid@mq.edu.au

the ratio between the line-of-sight velocity and the line-of-sight velocity dispersion, v/σ (Binney 1978). In the context of IFS stellar kinematics this is given as (Binney 2005, eq. 26):

$$v/\sigma = \sqrt{\frac{\sum_{i=1}^{N} F_i v_i^2}{\sum_{i=1}^{N} F_i \sigma_i^2}},$$
 (1)

where N is the number of spaxels in the chosen aperture, v_i is the line-of-sight velocity of a spaxel measured relative to the average line-of-sight velocity of the galaxy, σ_i is the line-of-sight velocity dispersion, and F_i is the flux in a band (typically chosen to match the wavelength region of extracted kinematics) for the i^{th} spaxel or spatial bin. For example, a galaxy with highly ordered stellar motions within a disc has a dominant velocity term relative to the dispersion, and a high overall v/σ . However, due to the surface-brightness weighting, the v/σ parameter is known to be limited in its ability to discriminate between kinematically distinct galaxy populations, such as galaxies with regular rotation across the galaxy scale radius and those with apparently 'decoupled' centrally rotating cores, leading to the development of the proxy for spin parameter, λ_R (Emsellem et al. 2007a). This parameter includes a radial weighting and is defined as:

$$\lambda_{R} = \frac{\sum_{i=1}^{N} F_{i} R_{i} |v_{i}|}{\sum_{i=1}^{N} F_{i} R_{i} \sqrt{v_{i}^{2} + \sigma_{i}^{2}}},$$
(2)

where R_i is the galactocentric radius for the i^{th} spaxel or spatial bin. There are different ways to define this radius; in this work R_i represents the semi-major axis of the ellipse on which the i^{th} spaxel lies, which follows galaxy light profiles more naturally than projected circular apertures (Cortese et al. 2016; van de Sande et al. 2017b). This λ_R metric was used to quantify galaxy kinematic classes in the pioneering IFS survey ATLAS^{3D} (Cappellari et al. 2011a), the first such survey of a statistical sample of resolved galaxies, and found that galaxies fall largely into two kinematic categories; 'slow rotators' and 'fast rotators' (Emsellem et al. 2011). This classification scheme uses both the observed λ_R value and projected ellipticity (ϵ) of the galaxy. Fast rotators span a wide range of ellipticities but have clear structure in their velocity fields, representing disc-like orbits, and have λ_R values between ~ 0.1 and ~ 1 . Slow rotators, in contrast, are rounder objects with no global, regular rotation signature and therefore have λ_R values close to zero. Slow rotators are also comparatively rarer, forming just ~ 10 per cent of the galaxy population in the local Universe (Brough et al. 2017; van de Sande et al. 2017a), with the most massive galaxies more likely to be slow rotators (Emsellem et al. 2011; Brough et al. 2017; Veale et al. 2017).

Hydrodynamical, cosmological simulations can probe the formation pathways for the slow and fast rotator galaxy populations, and propose mechanisms by which they change across time. Schulze et al. (2018) found that the slow rotator fraction increased from 8 percent at z = 2 to 30 per cent at z = 0 for early-type galaxies, using a sample of galaxies from the Magneticum Pathfinder simulations (Dolag 2015). The accumulation of slow rotators across cosmic time suggests that the mechanism that drives the transformation from fast to slow rotator happens more frequently at later times. One such driver could be successive gas-poor mergers, as suggested by Naab et al. (2014), who linked the observable kinematic features of a galaxy to their evolutionary pathway with a small sample of galaxies from a cosmological 'zoom' simulation. Results from 'Evolution and Assembly of GaLaxies and their Environments' (EAGLE) simulations (Crain et al. 2015; Schaye et al. 2015) also indicate that low spin galaxies generally experienced gas-poor mergers, whereas galaxies at z=0 with normal spin experienced either no mergers or gas-rich mergers. Major mergers in either category of gas-poor or gas-rich exaggerated these effects, with aligned gas-rich major mergers effectively spinning up galaxies (Lagos et al. 2018b). An observational study of the orbital distribution of galaxies using Schwarzschild dynamical modelling by Santucci et al. (2022) found that slow rotators assemble at early times and have evolutionary pathways dominated by gas-poor mergers, whereas fast rotators tend to grow via gas accretion. Overall, the evolution of λ_R within a galaxy population over cosmic time reflects the combination of the above processes, and can therefore be used as a probe of galaxy assembly.

Testing our understanding of the evolution of spin in galaxies is observationally challenging, as it requires spatially resolved spectra of the stellar continuum at increasingly higher redshifts. Here we present measurements of λ_R and v/σ from the 'Middle Ages Galaxy Properties with Integral field spectroscopy' (MAGPI) survey (Foster et al. 2021), which targets massive galaxies at a lookback time of 3-4 billion years, with resolution comparable to redshift zero surveys. By carefully comparing MAGPI galaxies to the local Universe 'Mapping Nearby Galaxies at Apache Point Observatory' (MaNGA) sample (Bundy et al. 2015), we test whether there has been a systematic change in the kinematic states of galaxies from the Universe's middle ages to now. This is an initial look at the evolution of λ_R with MAGPI, using the first ~ 60 per cent of objects available from the survey (34/56 fields). We leave explorations of environment and detailed comparisons to hydrodynamical, cosmological simulations to a future work.

In Section 2 we introduce the three data sets used to understand the evolution of λ_R across cosmic time; the MAGPI sample at $z\sim0.3$, the MaNGA sample at $z\sim0$, and the EAGLE simulation data used to connect them. In Section 3 we present our methods for measuring λ_R , sample selection, correcting for seeing effects, and how we make the comparison between MAGPI and MaNGA to account for progenitor bias. We discuss our results in Section 4 and present our conclusions in Section 5. To convert between angular and physical scales for MAGPI data in this work, we adopt a flat Λ CDM cosmology with $H_0=70~{\rm km\,s^{-1}Mpc^{-1}}$ and $\Omega_m=0.3$.

2 DATA

To understand the possible evolution in the proxy for spin parameter λ_R we compared a sample of MAGPI galaxies to a sample chosen from the MaNGA survey. To connect the two observational data sets across 4 Gyr of cosmic history we used the EAGLE simulations. We introduce each data set below.

2.1 MAGPI

The MAGPI survey² is a VLT/MUSE Large Program which targets galaxies at $z\sim0.3$. The 60 primary targets have stellar masses estimated at $M_{\star}>7\times10^{10}M_{\odot}$ and correspond to galaxies with spatially resolved stellar continuum spectroscopy. In addition to those, there are hundreds of foreground and background sources. The survey uses MUSE in the wide-field mode with spectra in the range 4650-9300~Å in steps of 1.25~Å per pixel, and ground-layer adaptive optics. We

¹ Based on observations obtained at the Very Large Telescope (VLT) of the European Southern Observatory (ESO), Paranal, Chile (ESO program ID 1104.B-0536)

https://magpisurvey.org

measure the PSF field by field; an indicative point-spread function (PSF) for the survey is ~ 0.6 arcsec, which is equivalent to 4.5 kpc at $z \sim 0.3$ with the assumed cosmology. Each field is observed across six observing blocks of 2×1230 s exposures with rotational dithers, with a total on-source integration time of 4.4 hours per field.

We provide a brief overview of the data reduction process, with full details to be given in Mendel et. al. (in prep.). Reduction is based on the MUSE reduction pipeline (Weilbacher et al. 2020), with sky-subtraction completed using Zurich Atmosphere Purge sky-subtraction software (Soto et al. 2016). Segmentation maps and estimates of galaxy structural parameters are created using ProFound (Robotham et al. 2018). Each source identified within a field is post-processed to be situated at the centre of a 'minicube' extracted from the main MUSE cube, which is sized to encompass the maximum extent of the dilated segmentation map determined by ProFound. This work uses data from spatially resolved primaries and secondaries within the 34 available MAGPI fields as of October 2023 with reduced data and team available data products. The cuts we use on these data are described in Section 3.3.

2.2 MaNGA

We use the λ_R and v/σ catalogue of Fraser-McKelvie & Cortese (2023) as the local Universe comparison sample, measured from the MaNGA survey. We chose MaNGA as the comparison sample because it contains a large number of high mass systems, allowing us to create random subsets of the sample that represent potential evolutionary endpoints of MAGPI galaxies, and has comparable physical resolution to the MAGPI survey (see Foster et al. 2021 figure 2).

The MaNGA survey observed over 10000 galaxies between redshifts 0.01 < z < 0.15, with spectral coverage of 3600 - 10300 ÅThe primary sample generally extends of ~ 1.5 half-light radii (Yan et al. 2015; Wake et al. 2017). Reduced and derived properties are available from the MaNGA Data Reduction Pipeline and MaNGA Data Analysis Pipeline, respectively (Law et al. 2015; Westfall et al. 2019). The average seeing conditions for the survey in the r-band give a PSF FWHM of ~ 2.5 arcsec.

Details on how the MaNGA values were measured can be found in Fraser-McKelvie & Cortese (2022). As with the MAGPI method described in Section 3.3, r-band measurements of λ_R and v/σ (defined in Eq. 1 and Eq. 2) were made by considering spaxels within the half-light ellipse, and corrected for seeing using the kinematic corrections code published by Harborne et al. $(2020)^4$. We took elliptical Petrosian half-light radii for MaNGA objects from the survey's data analysis pipeline summary table, drpall_v3_1_1. The MaNGA sample from the study by Fraser-McKelvie & Cortese (2022) includes 4741 objects at a median redshift of 0.04.

2.3 EAGLE

We use the EAGLE simulations to link our observed samples of galaxies by tracing the evolution of MAGPI-like EAGLE galaxies to the local Universe, described in Section 3.4. The purpose of using the EAGLE simulations is to account for the varied evolutionary pathways a galaxy might take between the Universe's middle ages

and present day, as opposed to adopting a simple stellar mass growth model.

We choose the EAGLE simulations because the galaxy stellar mass function has been shown to accurately match observations up to and beyond z=0.5 (Furlong et al. 2015), which comfortably includes the redshift span we consider in this work. We do not expect this choice of simulation to be critical, as there is only minor stellar mass growth between redshift 0.3 and redshift 0.

In particular, we use the cosmological hydrodynamic EAGLE reference model Ref-L100N1504 and the catalogue of stellar masses and λ_R values created by Lagos et al. (2018b). This reference model has gas particle mass of $1.8 \times 10^6 \, \mathrm{M_\odot}$ and dark matter particle mass of $9.7 \times 10^6 \, \mathrm{M_\odot}$, with a volume given by sides of $L = 100 \, \mathrm{cMpc^3}$. To trace between the MAGPI sample and MaNGA sample we use snapshot 25 at z = 0.27, which is closest to the nominated 0.3 target redshift of the MAGPI survey, and snapshot 28 corresponding z = 0 to link to the MaNGA sample. In total, the EAGLE sample comprises of 9409 galaxies traceable between the two redshifts, with stellar masses between $9.08 < \log_{10}(M_{\star}/\mathrm{M_\odot}) < 12.27$ at z = 0.

3 METHODS

In this section we describe the methods used on MAGPI objects to construct the 2D stellar kinematics and estimate the structural parameters, such as ellipticity and half-light radius, needed for the λ_R and v/σ measurements. We then describe how the observed values were corrected for seeing conditions, and the method used to account for progenitor bias when comparing the MAGPI galaxies at 3-4 Gyr lookback time to the local Universe MaNGA sample.

3.1 Stellar kinematics

Full details of the MAGPI kinematic extraction can be found in Mendel et. al. (in prep.), but we give a brief overview here. Stellar kinematics are obtained using a customised version of GISTPIPELINE⁷ v2.1 (Bittner et al. 2019) which uses PPXF⁸ for full-spectrum fitting (Cappellari & Emsellem 2004; Cappellari 2017). A reduced version of IndoUS is used for the stellar template library (Valdes et al. 2004). Spaxels within the ProFound derived half-light (R50) radius are co-added to construct an aperture spectrum, the fit of which provides the initial redshift estimate for the object.

A subset of templates for use in the fitting of individual spaxels is then determined using the method described in van de Sande et al. (2017b). For each object, a series of elliptical annuli are created, considering only spaxels with a signal-to-noise > 3. These annuli are centered on the galaxy and their ellipticity is determined from the Profound axis ratios. The annuli are grown by half a pixel until either the target signal-to-noise of 25 is reached, or there are no more valid spaxels to merge. The spectrum of each annular bin is fit and the non-zero weighted templates used in the fit of each annulus are stored.

Each individual spaxel is then fit using as input a reduced set of stellar templates, consisting of the templates used to fit the annuli to which the spaxel belongs, and the immediately adjacent annulii. Errors for each spaxel are determined using Monte Carlo simulations, whereby realisations of the input spectra were created by adding random noise based on the residuals of the fit.

³ https://github.com/asgr/ProFound

⁴ https://github.com/kateharborne/kinematic_corrections

⁵ https://www.sdss4.org/dr17/manga/manga-data/catalogs/

⁶ Catalogue values were accessed from Fraser-McKelvie & Cortese (2023).

⁷ https://abittner.gitlab.io/thegistpipeline/

⁸ https://pypi.org/project/ppxf/

3.2 Estimating structural parameters

Using r-band images created from the collapsed MUSE spectral cubes, we model the galaxy light with the Python package MGEFIT, which parameterises the light as a series of 2D Gaussians (Emsellem et al. 1994; Cappellari 2002); we refer to this model as a 'Multi-Gaussian Expansion' (MGE) in the text. Stacked point-sources in each MAGPI field are used to estimate the PSF (modelled with a circular MGE model) so that the resulting galaxy light models are PSF-deconvolved. From the optimal MGE fit we obtain the ellipse containing half the galaxy light, measuring its ellipticity ($\epsilon_e = 1$ – b/a, with a and b the semi-major and semi-minor axes, respectively) and semi-major axis, R_e . We use this half-light radius definition in all subsequent MAGPI analysis. We note the MGE method we use here is the same as that presented in Derkenne et al. (2023), which includes further details on the multi-Gaussian fitting process. This way of estimating the half-light radius is slightly different from the Petrosian half-light radius for the MaNGA sample, but we do not expect this difference to have a significant impact on our results.

Stellar masses for MAGPI objects are calculated using the spectral energy distribution fitting software PROSPECT¹⁰ with a Chabrier (2003) initial mass function. The spectral energy distribution is measured using 'Galaxy and Mass Assembly' (GAMA) survey imaging in the *ugriZYJHKs* bands, pixel-matched to MAGPI data in order to exactly correspond to MAGPI survey objects (Bellstedt et al. 2020). Sérsic indices are determined using GALFIT¹¹ (Peng et al. 2002) on the collapsed spectral cube images, modelling both the central galaxy and any neighbouring galaxies within five magnitudes. A single Sérsic component is used, with a local background subtracted prior to fitting.

3.3 Measuring λ_R and v/σ

We use Eq. 1 and Eq. 2 to measure v/σ and λ_R from the MAGPI data. In this work we choose the half-light ellipse as our aperture, with spaxel flux measured in the r-band. We denote λ_R and v/σ measured within the half-light ellipse as λ_{R_e} and $(v/\sigma)_e$, respectively. Valid spaxels are defined as having finite velocity and velocity dispersion values, with an uncertainty requirement on the velocity dispersion given by:

$$\Delta \sigma < 25 \text{ kms}^{-1} + 0.1\sigma, \tag{3}$$

which follows the data quality requirements used by van de Sande et al. (2017b).

Uncertainties on the λ_{R_e} and $(v/\sigma)_e$ values are estimated by creating realisations of the line-of-sight velocity and dispersion values based on their measured uncertainties from the full-spectrum fitting process, described in Section 3.1, and repeating the measurements 2000 times in a Monte-Carlo approach. The uncertainty is given as the standard deviation of the resulting distribution of measurement, divided by $\sqrt{2}$, since this process adds more noise to data that already has noise. As both λ_{R_e} and $(v/\sigma)_e$ are flux weighted quantities, typical uncertainties are small, with values of ~ 0.02 . We show two examples of the stellar kinematic fields used to make measurements of λ_{R_e} and $(v/\sigma)_e$ in Figure 1, with MAGPI object 1523197197 representing a typical slow rotator and MAGPI object 2310199196 representing a typical fast rotator.

Due to the redshift of the MAGPI survey targets, correcting the measured λ_{R_e} and $(v/\sigma)_e$ values for the effects of a point-spread function is important, as seeing conditions can artificially reduce observed values. We use the kinematic corrections code of Harborne et al. (2020) to correct our observed values to their intrinsic ones, based on how resolved each galaxy is, its Sérsic index, and ellipticity. We first selected all MAGPI objects with stellar masses $\log_{10}(M_{\star}/\mathrm{M}_{\odot}) > 10$. To ensure accurate seeing corrections we require that all galaxies have at least 50 spaxels within the half-light ellipse, with a fill fraction (total spaxel area divided by half-light ellipse area) of more than 85 per cent. We also require that the PSF dispersion (PSF FWHM/2.355) is less than 40 per cent of the semimajor axis of the half-light ellipse, and that the Sérsic index of each object is less than 8. as All candidate galaxies with λ_{R_a} and $(v/\sigma)_e$ measurements are shown in Figure 2. The final sample of MAGPI galaxies used for all subsequent analyses includes 51 objects.

We stress that the measurements of λ_{R_e} and $(v/\sigma)_e$ for MAGPI objects follows closely the methodology of Fraser-McKelvie & Cortese (2022), allowing for a fair comparison between the MAGPI and MaNGA observational samples (once progenitor bias and sample selection effects are accounted for - see Section 3.4). However, due to the redshift of the MAGPI sample, the rest-frame kinematics of the MAGPI sample are in a different band to those of MaNGA, and hence probe subtly different stellar populations. We expect the effect of this difference on the comparison of their λ_{R_e} distributions to be small

3.4 Accounting for progenitor bias

To measure the degree of evolution between galaxies in the middle ages of the Universe and today it is important to take into account progenitor bias (van Dokkum & Franx 1996). The MAGPI sample consists of massive galaxies at a lookback time of 3-4 Gyr, and so choosing a mass-matched sample of massive galaxies in the local Universe disregards any possible evolution in morphology, age, mass, and size that might have occurred across the intervening time. Furthermore, galaxy evolution is inherently stochastic, in the sense it is not deterministic that a particular type of galaxy at one epoch will exactly evolve into another type at later times. This problem has been tackled using hydrodynamical cosmological simulations and tracing the number density of galaxies through cosmic time (Torrey et al. 2015; Wellons & Torrey 2017). To account for the complexities of comparing galaxy populations across time we use a sampling method developed by Khalid et. al. (in prep.), who found that the major driver of progenitor bias is stellar mass. By accounting for evolution in stellar mass alone, through use of cosmological simulations, the evolution of parameters such as λ_R can be accurately inferred. This result is demonstrated in the above work.

Our implementation of this method is as follows. First, we estimate the probability density function (PDF) for stellar mass of the MAGPI galaxy sample. The PDF is estimated using Gaussian kernels and Silverman's rule for the bandwidth calculation, implemented through scipy (Virtanen et al. 2020). We also estimate the stellar mass PDF of the entire EAGLE sample at the redshift snapshot most similar to the MAGPI target redshift (z = 0.27). We then draw a random sample of EAGLE galaxies weighted by the ratio of the MAGPI PDF and EAGLE PDF, with the weighting factor w_1 given by:

$$w_1 = \frac{\text{PDF}(M_{\star,\text{MAGPI}})}{\text{PDF}(M_{\star,\text{EAGLE},z=0.27})}.$$
 (4)

Once normalised so that the probabilities sum to one, the weighting

⁹ https://pypi.org/project/mgefit/

¹⁰ https://github.com/asgr/ProSpect

¹¹ https://users.obs.carnegiescience.edu/peng/work/galfit/
galfit.html

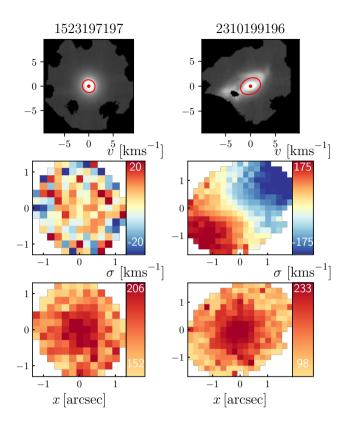


Figure 1. Left column: The top row shows the flux for MAGPI object 1523197197 with the half-light ellipse marked in red. The second row shows its stellar kinematic line-of-sight velocity field, which shows no clear rotation. The third row shows the stellar kinematic velocity dispersion field. Only spaxels within the half-light ellipse are shown. Right column: The same as the left column, but for MAGPI object 2310199196, which has a clear rotation signature in its line-of-sight velocity field.

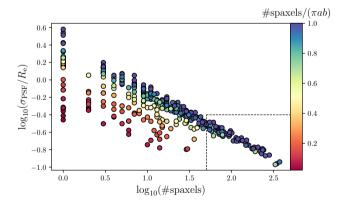


Figure 2. The (\log_{10}) number of spaxels within the half-light ellipse against the (\log_{10}) resolution, cast as PSF sigma over half-light radius, of all MAGPI objects with a valid λ_{R_e} and $(v/\sigma)_e$ measurement, coloured by fill-fraction (number of spaxels/area of half-light ellipse). These parameters primarily determine which galaxies can be accurately corrected from seeing-blurred λ_{R_e} and $(v/\sigma)_e$ values to intrinsic values (Harborne et al. 2020). The dashed lines show the cuts used in this work, for all galaxies with a fill fraction above 85 per cent.

factor on the randomly drawn EAGLE galaxies forces the sample to have the same statistical properties as the MAGPI one in terms of stellar mass. While the drawn EAGLE sample at this point can theoretically have almost arbitrary size, we match it to the MAGPI sample size to build in the effects of having a small number of objects on the end results.

EAGLE galaxies can be traced across snapshots by using a unique combination of group and sub-group IDs, and snapshot number. In this way we let the EAGLE sample evolve to redshift zero and remeasure the stellar mass PDF in the redshift zero snapshot. We again use weights (w_2) to randomly draw MaNGA galaxies and force the drawn sample to have the same underlying stellar mass statistics as the evolved EAGLE sample:

$$w_2 = \frac{\text{PDF}(M_{\star, \text{EAGLE sample}, z=0})}{\text{PDF}(M_{\star, \text{MaNGA}})}.$$
 (5)

The drawn MaNGA sample represents a possible evolutionary pathway of the MAGPI sample as informed by the EAGLE simulations. However, as noted above, the evolutionary pathways of galaxies are not deterministic, and so a single measurement can only represent one outcome among many. To statistically explore the possible evolutionary scenarios, we repeat the sampling method (randomly re-selecting the EAGLE galaxies to trace, and the local sample of MaNGA galaxies) 100 times to understand the distribution of outcomes, which we present in Section 4. No cuts are made on the sample in terms of age, star formation rate, or morphology, so that each drawn sample contains a mixture of galaxies. We show the stellar mass and half-light size distribution of the MAGPI galaxies and all drawn MaNGA galaxies in Figure 3.

We should note that we have only accounted for stellar mass when choosing a MaNGA sample designed to avoid progenitor bias. Tracing by stellar mass alone only works if the MAGPI sample is representative in its physical parameters compared to the EAGLE one at the same epoch. One key point worth further consideration is that the amount of mass growth an EAGLE galaxy experiences is proportional to its star formation rate, as shown in figure 11 of Croom et al. (2021), and galaxy kinematics can also depend on star formation rate Wang et al. (2020). Star-forming galaxies tend to undergo a greater mass growth than passive galaxies for z < 1, and so if the MAGPI sample is over-represented in star-forming objects compared to the EAGLE simulations, we might expect to be slightly biased in the traced mass growth.

To explore this issue, we characterise the MAGPI sample by using offsets (i.e. distance) from the star-forming main sequence as measured from spectral diagnostics in the MAGPI MUSE data (Mun et al. 2024). The classifications are defined using the following intervals in star formation rate (SFR) from Mun et al. (2024):

• Star-burst: Δ SFR > 0.5 dex

Main-sequence: -0.5 dex < ΔSFR < 0.5 dex
 Green-valley: -1.1 dex < ΔSFR < -0.5 dex

• Passive: Δ SFR < -1.1 dex

For the sample used in this work, we find 21 objects that are either star-burst, main-sequence, or 'green-valley' objects, and 30 passive objects. This breakdown is similar to the 40-60 per cent of passive galaxies at the relevant mass range in the EAGLE simulations for $z \sim 0.1-1$ (Furlong et al. 2015). We conclude the MAGPI sample is not over-represented in star-forming objects with respect to the EAGLE simulations for stellar masses $\log_{10} M_{\star}/M_{\odot} > 10$. A more complete treatment of the nuanced relationships between stel-

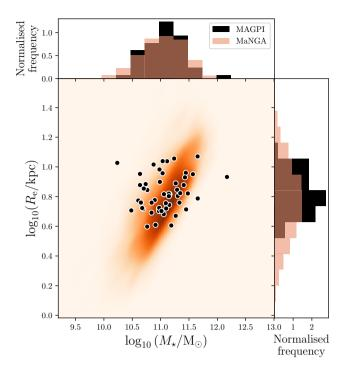


Figure 3. The half-light radius, defined as the semi-major axis of ellipse containing half the galaxy light, against the stellar mass of the MAGPI and MaNGA samples used in this work. All 100 random draws from the MaNGA sample are shown as the background 2D kernel density estimate in orange. The MAGPI sample has a particularly massive object that has no such massive counterpart in the MaNGA sample.

lar mass, star formation rate, and λ_R might be possible with the full MAGPI sample.

4 RESULTS AND DISCUSSION

We show the λ_{R_e} distribution against galaxy half-light ellipticity for the MAGPI galaxies in Figure 4. The seeing-corrected values are always higher than the uncorrected values, with smaller corrections typical for lower λ_{R_e} values. We find a few objects at the extreme end of the distribution, with $\lambda_{R_e} > 0.8$ and ellipticity greater than ~ 0.6 , which represent fast rotating, highly flattened systems, and typically tend to be Sb or Sc in their Hubble type (Falcón-Barroso et al. 2019). One object has a notably high corrected λ_{R_e} value of ~ 1 , which implies negligible dispersion compared to stellar rotation, and could be due to uncertainties on the correction process itself (Harborne et al. 2020).

We use the cuts proposed by Cappellari (2016) to discriminate between fast rotators and the rarer population of slow rotating galaxies, as we found this boundary to well separate the slow and fast rotators for the MAGPI sample, based on visual inspection of the velocity fields. However, we note that for the 'Sydney-AAO Multi-object Integral field spectrograph survey' (SAMI; Croom et al. 2012), a slightly larger region was identified as being optimal when classifying slow rotators (van de Sande et al. 2021). Given this difference between surveys there is not a strict universal region inhabited by purely slow rotating galaxies, and the choice of region should be driven by the actual kinematics of the galaxies in the sample. The seeing correction may also over-correct slow-rotating galaxies, so the definition chosen

has subtle impact on the fraction of slow rotators found (van de Sande et al. 2021). Using the Cappellari (2016) metric, a slow rotator has:

$$\lambda_{R_e} < 0.08 + \epsilon_e/4 \text{ with } \epsilon_e < 0.4.$$
 (6)

In the MAGPI sample we find a slow rotator fraction of $18^{+6.6}_{-4.1}$ per cent (9/51 objects), with uncertainty estimated using the binomial distribution uncertainty estimate technique from Cameron (2011). Without seeing corrections applied, we find a slow rotator fraction of $24^{+0.6}_{-10}$ per cent (12/51 objects), and so the applied corrections do not significantly impact our conclusions. We compare the MAGPI fraction to slow rotator fractions derived from the selected MaNGA samples using the same cuts, shown in Figure 5. The MaNGA sample across 100 draws has a similar slow rotator fraction at 19 per cent with a standard deviation of 6 per cent. However, the lowest slow rotator fraction observed in the MaNGA sample is ~ 5 per cent, and the largest is ~ 30 per cent, which hints at the pitfalls of comparing small samples in a non-probabilistic manner. Given this large range of possible slow rotator fractions, taking any single draw of the MaNGA sample could lead to interpreting a dramatic evolution in the λ_{R_e} parameter, whereas the distribution of samples does not support such an evolution.

The entire λ_{R_e} distribution can also be compared between the two observational samples, as shown in Figure 6. The cumulative distribution function (CDF) of the MAGPI sample generally falls within the one-sigma region of the MaNGA drawn samples, except at λ_{R_e} values greater than ~ 0.6, where the MAGPI sample shows an excess of higher λ_{R_c} values compared to the MaNGA sample. This is potentially a hint of the fast rotating population spinning down between redshift 0.3 and the local Universe; however statistically the distributions are not separable. We use an Anderson-Darling test statistic to determine if each of the drawn MaNGA samples and the observed MAGPI sample could be drawn from the same underlying probability distribution, as this statistical test is particularly sensitive to the tails of distributions (Scholz & Stephens 1987). We use an alpha value for significance of 0.01, and across the 100 random draws fail to reject the null hypothesis (that the observed samples are drawn from the same underlying distribution) in 93 per cent of cases.

We then explore only MaNGA and MAGPI λ_{R_e} values above 0.5, where the difference is most pronounced, and repeat the statistical tests. Across 100 random draws we fail to reject the null hypothesis in 82 per cent of cases. Although visually there appears to be a significant difference between the distributions at high λ_{R_e} , we note that we have the benefit of being able to randomly draw MaNGA samples and thus construct an understanding of the variance of the distributions, whereas we have only one MAGPI sample to compare against. There are also very few galaxies at the very high lambda end where the difference is visually most striking (11 with $\lambda_{R_e} > 0.8$ in MAGPI). These small number statistics also make it difficult to form strong conclusions about this high λ_{R_e} trail in MAGPI relative to the MaNGA sample, with statistical tests unlikely to reject the null hypothesis. However, the hint of a difference remains interesting and worthy of future exploration with the complete MAGPI sample.

The high λ_{R_c} tail observed in the MAGPI distribution is also partly a function of the kinematic corrections applied to the MAGPI data, which we point out is not without uncertainty. Harborne et al. (2020) note a residual 1σ scatter of ~ 0.02 dex in λ_{R_c} after trends in ellipticity, aperture, and Sérsic index are accounted for. Realistically these errors are probably larger for the MAGPI sample, as the kinematic corrections code assumes no uncertainty (or very highly resolved) photometric parameters.

In Figure 7 we show the relationship between λ_{R_e} and $(v/\sigma)_e$ for MAGPI galaxies compared to the randomly drawn MaNGA galax-

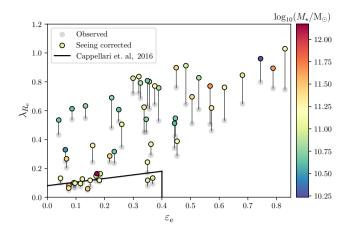


Figure 4. The proxy for spin parameter, λ_{Re} , against ellipticity, ϵ_{e} , both measured within the half-light ellipse, for the MAGPI sample. Objects in the lower left corner are round and pressure supported. Objects in the upper right corner are highly flattened with ordered stellar motions. The observed values are shown in grey, with the seeing-corrected values shown coloured by their stellar mass. The cut between the fast rotating and rarer slow rotating population is shown in black, following Cappellari (2016). The cut definition is given in Eq. 6.

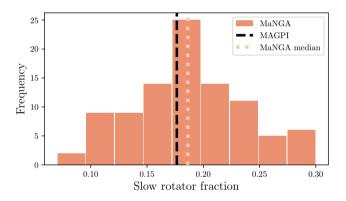


Figure 5. The slow rotator fraction of the MAGPI sample is shown as a black dashed line. All slow rotator fractions from the 100 drawn MaNGA samples are shown as a histogram with median of 19 per cent and standard deviation of 6 per cent. The median is marked by the orange dotted line.

ies. As in Emsellem et al. (2007b) equation B1, we relate the λ_R parameter to v/σ by:

$$\lambda_R = \frac{\langle RV \rangle}{\langle R\sqrt{(v^2 + \sigma^2)}} \approx \frac{\kappa(v/\sigma)}{\sqrt{1 + \kappa^2(v/\sigma)^2}}.$$
 (7)

The best-fitting κ value for MAGPI is 1.17 ± 0.03 , compared to the MaNGA value of 1.04 ± 0.002 . As with the λ_{R_e} cumulative distribution, we find that there exists a slight separation for the higher spin objects. At the same $(v/\sigma)_e$, MAGPI galaxies tend to have higher λ_{R_e} values than MaNGA galaxies for $(v/\sigma)_e$ values greater than ~ 0.6 .

The agreement of slow rotator fractions between the MAGPI and MaNGA samples, when explicitly accounting for progenitor bias, indicates that the population of slow rotators was already in place in the Universe's middle ages, and has not increased in the past 3-4

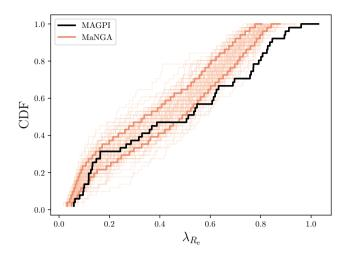


Figure 6. The cumulative distribution function of the MAGPI sample is shown as the black solid line. Each of the 100 random MaNGA draws are shown in light orange, with the 16^{th} and 84^{th} percentiles of the distribution at each λ_R value shown as a bold orange line. For most of the distribution, the MAGPI values fall within the 1σ region of the MaNGA draws, except for very high spin galaxies.

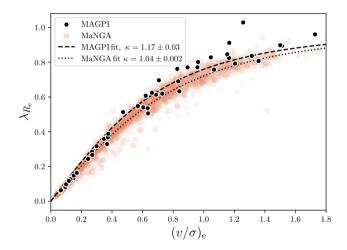


Figure 7. The relationship between λ_{R_c} and $(v/\sigma)_c$ for MAGPI galaxies in black and MaNGA galaxies in orange. The dashed line shows the best fit of Eq. 7 for MAGPI objects, with the dotted line for all MaNGA objects across the 100 draws.

Gyr of cosmic time. Given that simulations predict the slow rotator population builds up primarily due to dry mergers (Lagos et al. 2018b), our result suggests the mechanism of dry mergers primarily occurred earlier in the Universe's history for massive galaxies.

We note however that our analysis, by construction, is limited to exploring kinematics within the half-light radius only, and does not preclude changes to the stellar kinematics that may have occurred at larger radial scales. However, obtaining a large sample out to multiple half-light radii at this redshift remains challenging. Furthermore, we have necessarily limited the MAGPI sample to well resolved (less compact) galaxies in order to make accurate measurements of λ_{R_e} . Compact galaxies typically have similar λ_{R_e} values compared to their less compact counterparts (Cappellari et al. 2013), but their absence

from the sample could increase the importance of the massive galaxies in the distribution we study, with massive galaxies more likely to be slow rotators (Emsellem et al. 2011; Veale et al. 2017). This potential bias is a limitation of studying the kinematics of galaxies beyond the local Universe.

When selecting comparison samples, we have made no consideration of the potentially different environments of MAGPI and MaNGA galaxies. A positive correlation has been noted between the fraction of slow rotators and environmental density in some studies (Cappellari et al. 2011b; Fogarty et al. 2014), but it is unclear whether this is actually due to an underlying correlation between stellar *mass* and environment instead (Brough et al. 2017; Greene et al. 2017), where as noted above, more massive galaxies are more likely to be slow rotators. Recently, Vaughan et al. (2024) used a generalised linear model with binary classification to understand the relationship between environmental surface density and the kinematic classes of SAMI galaxies. They found that at fixed stellar mass, environmental surface density is not a useful predictor for the kinematic class of a galaxy. Future work on a larger sample will be needed to understand if this is also the case for MAGPI galaxies.

We report that the population of massive slow rotating galaxies was already in place at $z\sim0.3$, which is tension with the predictions of the Magneticum Pathfinder simulations (Dolag 2015). Schulze et al. (2018) in particular predict quite a strong build up of the slow rotator population using Magneticum simulation early-type galaxies. Between redshift 2 and 0, the frequency of slow rotators changes from 8 to 30 per cent, respectively, with an appreciable accumulation of slow rotators between redshifts 0.5 and 0 (see their figure 6). A slow rotator fraction of 30 per cent at redshift zero is larger than the MaNGA slow rotator fraction in this work of 19 per cent, and of local Universe slow rotator fraction estimates more generally (Emsellem et al. 2011; van de Sande et al. 2017b; Fraser-McKelvie & Cortese 2022). Some of the stronger evolution seen by Schulze et al. (2018) may be due to the sample of early-types used.

Schulze et al. (2018) also note a general trend of fast rotator galaxies redistributing stellar angular momentum across cosmic time, in that the entire population shifts towards lower λ_R values as redshift approaches zero. In the Magneticum Pathfinder simulations this shift happens both gradually, across the entire span from z = 2 to z = 0, and suddenly, whereby a galaxy transitions from a fast rotator to a slow rotator in less than 0.5 Gyr under the action of a major merger (Schulze et al. 2018).

In a detailed comparison of the slow rotator fractions from different hydrodynamical cosmological simulations, van de Sande et al. (2018) found that in general the simulation slow rotator fractions do not match the observed distributions well. This could be due to the many effects that impact how an observed λ_R measurement is made compared to a λ_R measurement on a simulated galaxy. Some of these effects can be alleviated through software like SIMSPIN (Harborne et al. 2023), which can generate mock IFS data from cosmological simulations in a consistent manner.

If the relatively higher MAGPI λ_{R_e} values compared to MaNGA are indicative of a subtle difference in their intrinsic distributions, it is interesting to speculate that the higher λ_{R_e} objects might then be more sensitive to whatever mechanism causes the change in how stellar angular momentum is distributed across time. As mentioned above, high λ_{R_e} objects tend to be spirals in morphological type (e.g. Falcón-Barroso et al. 2019), and so this could be an indication of disc fading (Croom et al. 2021) or an uneven effect of the efficiency of

dry mergers on galaxy spin. Speculation aside, we stress again that although there is an excess of high $\lambda_{R_{\rm e}}$ MAGPI objects compared to MaNGA ones, we do not find a statistically significant difference between the sample distributions and therefore conclude that there has not been a significant change in $\lambda_{R_{\rm e}}$ values across this time.

An analysis of the excess kurtosis of the stellar velocity distribution profile, h_4 , by D'Eugenio et al. (2023), found that there is 7σ evidence of a change in h_4 between redshifts 0.8 and 0 for quiescent galaxies with $\log_{10}(M_{\star}/\mathrm{M}_{\odot}) > 11$. The result suggests stellar anisotropy has increased gradually over cosmic time, perhaps due to minor mergers depositing ex-situ stars at large radii, with evolution occurring possibly as early as z = 0.8. D'Eugenio et al. (2023) note their result is slightly in tension with the predictions of the EAGLE simulations, which predict apparent galaxy spin down occurs mainly at z < 0.5 (Lagos et al. 2018a). The results of this work, where we note only a marginal excess of high λ_{R_e} values at z = 0.3 compared to local Universe values, are consistent with the conclusion of D'Eugenio et al. (2023), in that it suggests evolution of the stellar orbital structure occurred at earlier times. Likewise, Bezanson et al. (2018) compared the rotational support of quiescent galaxies at $z \sim 0.8$ and local galaxies, finding that galaxies at $z \sim 0.8$ had 94 per cent more rotational support at a radius of 5 kpc than their local counterparts, possibly due to a combination of dissipationless merging and the mechanism that ceases star formation. Galaxies at even early times $(z \sim 2)$ typically tend to be fast rotators, inferred both from their apparent shapes (van der Wel et al. 2011), and also their kinematics (Newman et al. 2018), implying there must be an accumulation of slow rotators at some point in the intervening time between the early Universe and present day.

5 CONCLUSIONS

We compare a sample of 51 massive MAGPI galaxies at a lookback time of 3-4 Gyr to carefully drawn samples of MaNGA galaxies in the local Universe to determine whether there has been a significant change in the stellar kinematic state of galaxies across this time. We quantify the kinematic state of a galaxy through its λ_{R_e} parameter, which is an observational proxy for spin. We use the EAGLE cosmological, hydrodynamical simulations to draw samples of galaxies mass-matched to our MAGPI sample at z=0.3, and trace them through time to z=0. This allows us to draw samples of local galaxies from the MaNGA survey to compare the λ_{R_e} distribution at $z\sim0$, accounting for progenitor bias and the diverse and stochastic evolutionary pathways a galaxy can follow across its history. We analyse the MAGPI λ_{R_e} distribution against 100 drawn MaNGA λ_{R_e} samples.

We assess whether the slow rotator population (using the definition of Cappellari 2016) has changed from the middles ages of the Universe to now. We find a slow rotator fraction of 18 per cent in our MAGPI sample. This is consistent with the median slow rotator fraction from the mass-evolved MaNGA samples, found to be 19 ± 6 per cent. Our results indicate there has been no significant evolution of the slow rotator fraction over the past 3-4 Gyr, as uniquely probed by MAGPI. We conclude that the massive ($\log_{10} M_{\star}/M_{\odot} > 10$) slow rotator population of galaxies was already in place at $z \sim 0.3$, and has not accumulated significantly since then. This result is an important calibration for models of galaxy evolution.

Finally, we compare the overall distribution of $\lambda_{R_{\rm e}}$ values between the MAGPI sample and the 100 drawn MaNGA samples. The MAGPI cumulative distribution of $\lambda_{R_{\rm e}}$ falls within the 1- σ expected range of the MaNGA draws for $\lambda_{R_{\rm e}} < 0.6$. Above this, there is a slight

¹² https://github.com/kateharborne/SimSpin

excess in the MAGPI λ_{R_c} values compared to MaNGA ones, which hints that the fastest rotating galaxies may, on average, have spun down in the intervening time. However, the distributions are not statistically separable using an Anderson-Darling test statistic. The possible evolution of λ_{R_c} at earlier times will be interesting to explore in future work with the full MAGPI sample for this epoch. The epoch at which the current slow rotator population became established may yet be explored by pushing resolved stellar kinematic studies to high redshifts with the benefit of instruments such as the JWST, and ground-based instruments such as the 'MCAO Assisted Visible Imager and Spectrograph' (MAVIS; McDermid et al. 2020).

ACKNOWLEDGEMENTS

We warmly thank the reviewer for their comments which helped improve this work. We wish to thank the ESO staff, and in particular the staff at Paranal Observatory, for carrying out the MAGPI observations. MAGPI targets were selected from GAMA. GAMA is a joint European-Australasian project based around a spectroscopic campaign using the Anglo-Australian Telescope. GAMA was funded by the STFC (UK), the ARC (Australia), the AAO, and the participating institutions. GAMA photometry is based on observations made with ESO Telescopes at the La Silla Paranal Observatory under programme ID 179.A-2004, ID 177.A-3016. The MAGPI team acknowledge support by the Australian Research Council Centre of Excellence for All Sky Astrophysics in 3 Dimensions (ASTRO 3D), through project number CE170100013. CF is the recipient of an Australian Research Council Future Fellowship (project number FT210100168) funded by the Australian Government. CL, JTM and CF are the recipients of ARC Discovery Project DP210101945. GS acknowledges funding from the Australian Research Council (ARC) Discovery Project DP210101945. AFM acknowledges support from RYC2021-031099-I and PID2021-123313NA-I00 of MICIN/AEI/10.13039/501100011033/FEDER, UE, NextGenerationEU/PRT. FDE acknowledges support by the Science and Technology Facilities Council (STFC), by the ERC Advanced Grant 695671 "QUENCH", and by the UKRI Frontier Research grant RISEandFALL. FDE is grateful to C. Conroy for sharing the high-resolution C3K/MIST library. JvdS acknowledges support of an Australian Research Council Discovery Early Career Research Award (project number DE200100461) funded by the Australian Government. Y.P. acknowledges the support from the National Science Foundation of China (NSFC) grant Nos. 12125301, 12192220, 12192222, and the science research grants from the China Manned Space Project with No. CMS-CSST-2021-A07. SMS acknowledges funding from the Australian Research Council (DE220100003). LMV acknowledges support by the German Academic Scholarship Foundation (Studienstiftung des deutschen Volkes) and the Marianne-Plehn-Program of the Elite Network of Bavaria.

DATA AVAILABILITY

The MAGPI spectral data underlying this work are available from the ESO Science Archive Facility (http://archive.eso.org/cms.html).

REFERENCES

Bellstedt S., et al., 2020, MNRAS, 496, 3235 Bezanson R., et al., 2018, ApJ, 858, 60

```
Binney J., 1978, MNRAS, 183, 501
Binney J., 2005, MNRAS, 363, 937
Bittner A., et al., 2019, A&A, 628, A117
Brough S., et al., 2017, ApJ, 844, 59
Bundy K., et al., 2015, ApJ, 798, 7
Cameron E., 2011, Publ. Astron. Soc. Australia, 28, 128
Cappellari M., 2002, MNRAS, 333, 400
Cappellari M., 2016, ARA&A, 54, 597
Cappellari M., 2017, MNRAS, 466, 798
Cappellari M., Emsellem E., 2004, PASP, 116, 138
Cappellari M., et al., 2011a, MNRAS, 413, 813
Cappellari M., et al., 2011b, Monthly Notices of the Royal Astronomical
    Society, 416, 1680
Cappellari M., et al., 2013, MNRAS, 432, 1862
Chabrier G., 2003, PASP, 115, 763
Cortese L., et al., 2016, MNRAS, 463, 170
Crain R. A., et al., 2015, MNRAS, 450, 1937
Croom S. M., et al., 2012, Monthly Notices of the Royal Astronomical Society,
Croom S. M., et al., 2021, MNRAS, 505, 2247
D'Eugenio F., et al., 2023, MNRAS, 525, 2789
Derkenne C., et al., 2023, MNRAS, 522, 3602
Dolag K., 2015, in IAU General Assembly. p. 2250156
Emsellem E., Monnet G., Bacon R., 1994, A&A, 285, 723
Emsellem E., et al., 2007a, MNRAS, 379, 401
Emsellem E., et al., 2007b, MNRAS, 379, 401
Emsellem E., et al., 2011, MNRAS, 414, 888
Falcón-Barroso J., et al., 2019, A&A, 632, A59
Fogarty L. M. R., et al., 2014, Monthly Notices of the Royal Astronomical
    Society, 443, 485
Foster C., et al., 2021, Publ. Astron. Soc. Australia, 38, e031
Fraser-McKelvie A., Cortese L., 2022, ApJ, 937, 117
Fraser-McKelvie A., Cortese L., 2023, VizieR Online Data Catalog, p.
Furlong M., et al., 2015, MNRAS, 450, 4486
Greene J. E., et al., 2017, The Astrophysical Journal Letters, 851, L33
Harborne K. E., van de Sande J., Cortese L., Power C., Robotham A. S. G.,
    Lagos C. D. P., Croom S., 2020, MNRAS, 497, 2018
Harborne K. E., et al., 2023, Publ. Astron. Soc. Australia, 40, e048
Lagos C. d. P., et al., 2018a, MNRAS, 473, 4956
Lagos C. d. P., Schaye J., Bahé Y., van de Sande J., Kay S. T., Barnes D.,
    Davis T. A., Dalla Vecchia C., 2018b, MNRAS, 476, 4327
Law D. R., et al., 2015, The Astronomical Journal, 150, 19
McDermid R. M., et al., 2020, arXiv e-prints, p. arXiv:2009.09242
Mun M., et al., 2024, MNRAS,
Naab T., et al., 2014, MNRAS, 444, 3357
Newman A. B., Belli S., Ellis R. S., Patel S. G., 2018, ApJ, 862, 126
Peng C. Y., Ho L. C., Impey C. D., Rix H.-W., 2002, AJ, 124, 266
Robotham A. S. G., Davies L. J. M., Driver S. P., Koushan S., Taranu D. S.,
    Casura S., Liske J., 2018, MNRAS, 476, 3137
Santucci G., et al., 2022, ApJ, 930, 153
Schaye J., et al., 2015, MNRAS, 446, 521
Scholz F. W., Stephens M. A., 1987, Journal of the American Statistical
    Association, 82, 918
Schulze F., Remus R.-S., Dolag K., Burkert A., Emsellem E., van de Ven G.,
    2018, MNRAS, 480, 4636
Soto K. T., Lilly S. J., Bacon R., Richard J., Conseil S., 2016, MNRAS, 458,
Torrey P., et al., 2015, Monthly Notices of the Royal Astronomical Society,
```

Valdes F., Gupta R., Rose J. A., Singh H. P., Bell D. J., 2004, ApJS, 152, 251

Vaughan S. P., et al., 2024, Monthly Notices of the Royal Astronomical

Veale M., Ma C.-P., Greene J. E., Thomas J., Blakeslee J. P., McConnell N.,

Wang B., Cappellari M., Peng Y., Graham M., 2020, MNRAS, 495, 1958

Walsh J. L., Ito J., 2017, MNRAS, 471, 1428

Wake D. A., et al., 2017, The Astronomical Journal, 154, 86

Virtanen P., et al., 2020, Nature Methods, 17, 261

454 2770

Society, 528, 5852

10 Derkenne et al.

Weilbacher P. M., et al., 2020, A&A, 641, A28
Wellons S., Torrey P., 2017, MNRAS, 467, 3887
Westfall K. B., et al., 2019, The Astronomical Journal, 158, 231
Yan R., et al., 2015, The Astronomical Journal, 151, 8
van Dokkum P. G., Franx M., 1996, MNRAS, 281, 985
van de Sande J., et al., 2017a, MNRAS, 472, 1272
van de Sande J., et al., 2017b, ApJ, 835, 104
van der Wel A., et al., 2011, ApJ, 730, 38
van de Sande J., et al., 2018, Monthly Notices of the Royal Astronomical Society, 484, 869
van de Sande J., et al., 2021, Monthly Notices of the Royal Astronomical Society, 505, 3078

This paper has been typeset from a TEX/IATEX file prepared by the author.